



**A Surface-Tailored, Purely Electronic, Mott
Metal-to-Insulator Transition**

R. G. Moore, *et al.*

Science **318**, 615 (2007);

DOI: 10.1126/science.1145374

**The following resources related to this article are available online at
www.sciencemag.org (this information is current as of October 25, 2007):**

Updated information and services, including high-resolution figures, can be found in the online version of this article at:

<http://www.sciencemag.org/cgi/content/full/318/5850/615>

Supporting Online Material can be found at:

<http://www.sciencemag.org/cgi/content/full/318/5850/615/DC1>

This article appears in the following **subject collections**:

Physics, Applied

http://www.sciencemag.org/cgi/collection/app_physics

Information about obtaining **reprints** of this article or about obtaining **permission to reproduce this article** in whole or in part can be found at:

<http://www.sciencemag.org/about/permissions.dtl>

neutral parts of a disk (27), allowing solids to diffuse outward around the midplane while still avoiding the inward flows that would frustrate their transport to the outer disk. The only requirement for this model is that the disk was hot enough to process materials at the needed temperatures. Although high mass accretion rates are initially needed to produce these temperatures, the rates that are needed to deliver large amounts of high-temperature materials to the outer disk are typical for young T-Tauri stars (11) and more than an order of magnitude less than required by previous models (3).

An important consequence of this model is that the thermally processed grains would have remained in contact with the nebular gas throughout their transport, allowing volatiles to condense on their surfaces in cooler environments. In the X-wind model (28), grains are processed by radiation from the Sun as they are launched above the disk in bipolar outflows. These grains would have lost their volatiles upon being heated, then decoupled from the gas to rain back onto the solar nebula. As these grains fell onto the solar nebula in the comet-formation region, there would be mixing between two components: the solar composition materials that were already present and the more refractory crystalline grains.

Thus, comets that grew from these materials would be depleted in volatile elements, and those depletions would correlate with the amount of crystalline materials they contain. Preliminary analyses of the Stardust samples indicate that Comet Wild 2 exhibits no such depletions (29).

References and Notes

1. F. Kemper, W. J. Vriend, A. G. G. M. Tielens, *Astrophys. J.* **609**, 826 (2004).
2. J. A. Nuth III, H. G. M. Hill, G. Kletetschka, *Nature* **406**, 275 (2000).
3. D. Bockelée-Morvan, D. Gautier, F. Hersant, J.-M. Hure, F. Robert, *Astron. Astrophys.* **384**, 1107 (2002).
4. S. L. Hallenbeck, J. A. Nuth III, R. N. Nelson, *Astrophys. J.* **535**, 247 (2000).
5. D. Brownlee *et al.*, *Science* **314**, 1711 (2006).
6. M. E. Zolensky *et al.*, *Science* **314**, 1735 (2006).
7. K. D. McKeegan *et al.*, *Science* **314**, 1724 (2006).
8. G. J. MacPherson, D. A. Wark, J. T. Armstrong, in *Meteorites and the Early Solar System*, J. F. Kerridge, M. S. Matthews, Eds. (Univ. of Arizona Press, Tucson, 1988), pp. 746–807.
9. R. van Boekel *et al.*, *Nature* **432**, 479 (2004).
10. D. Apai *et al.*, *Science* **310**, 834 (2005).
11. L. Hartmann, N. Calvet, E. Gullbring, P. D'Alessio, *Astrophys. J.* **495**, 385 (1998).
12. J. E. Pringle, *Annu. Rev. Astron. Astrophys.* **19**, 137 (1981).
13. S. A. Balbus, J. F. Hawley, *Astrophys. J.* **376**, 214 (1991).
14. H.-P. Gail, *Astron. Astrophys.* **378**, 192 (2001).
15. Y. Amelin, A. N. Krot, I. D. Hutcheon, A. A. Ulyanov, *Science* **297**, 1678 (2002).

16. O. Hubickyj, P. Bodenheimer, J. J. Lissauer, *Icarus* **179**, 415 (2005).
17. A. P. Boss, *Science* **276**, 1836 (1997).
18. J. N. Cuzzi, S. S. Davis, A. R. Dobrovolskis, *Icarus* **127**, 290 (2003).
19. J. N. Cuzzi, S. J. Weidenschilling, in *Meteorites and the Early Solar System II*, D. S. Lauretta, H. Y. McSween Jr., Eds. (Univ. of Arizona Press, Tucson, 2006), pp. 353–381.
20. V. A. Urpin, *Sov. Astron.* **28**, 50 (1984).
21. T. Takeuchi, D. N. C. Lin, *Astrophys. J.* **581**, 1344 (2002).
22. Ch. Keller, H.-P. Gail, *Astron. Astrophys.* **415**, 1177 (2004).
23. Materials and methods are available as supporting material on Science Online.
24. R. Hueso, T. Guillot, *Astron. Astrophys.* **442**, 703 (2005).
25. C. P. Dullemond, C. Dominik, *Astron. Astrophys.* **434**, 971 (2005).
26. C. F. Gammie, *Astrophys. J.* **457**, 355 (1996).
27. B. Mukhopadhyay, N. Afshordi, R. Narayan, *Astrophys. J.* **629**, 383 (2005).
28. F. H. Shu, H. Shang, T. Lee, *Science* **271**, 1545 (1996).
29. G. J. Flynn *et al.*, *Science* **314**, 1731 (2006).
30. I thank J. Chambers, J. Cuzzi, and J. Nuth for suggestions that led to improvements to this manuscript. This research was supported by funds from the Carnegie Institution of Washington.

Supporting Online Material

www.sciencemag.org/cgi/content/full/318/5850/613/DC1
Materials and Methods
References

2 July 2007; accepted 25 September 2007
10.1126/science.1147273

A Surface-Tailored, Purely Electronic, Mott Metal-to-Insulator Transition

R. G. Moore,¹ Jiandi Zhang,^{2,3} V. B. Nascimento,¹ R. Jin,³ Jiandong Guo,¹ G.T. Wang,⁴ Z. Fang,⁴ D. Mandrus,³ E. W. Plummer^{1,3}

Mott transitions, which are metal-insulator transitions (MITs) driven by electron-electron interactions, are usually accompanied in bulk by structural phase transitions. In the layered perovskite $\text{Ca}_{1.5}\text{Sr}_{0.1}\text{RuO}_4$, such a first-order Mott MIT occurs in the bulk at a temperature of 154 kelvin on cooling. In contrast, at the surface, an unusual inherent Mott MIT is observed at 130 kelvin, also on cooling but without a simultaneous lattice distortion. The broken translational symmetry at the surface causes a compressional stress that results in a 150% increase in the buckling of the Ca/Sr-O surface plane as compared to the bulk. The Ca/Sr ions are pulled toward the bulk, which stabilizes a phase more amenable to a Mott insulator ground state than does the bulk structure and also energetically prohibits the structural transition that accompanies the bulk MIT.

The insulating phase associated with metal-insulator transitions (MITs) (1–4) can be described as either a band insulator (such as silicon) or a Mott insulator (such as nickel oxide). A band insulator has an even number of electrons per unit cell that can be described adequately by an independent electron theory, where all of the bands are either filled or empty at

0 K. If the number of electrons in the unit cell is odd, then band theory always predicts metallicity, but when the onsite Coulomb interaction (U) is comparable in magnitude to the bandwidth (W), the material can become a Mott insulator (1, 2). A transition from the Mott insulating phase to the metallic phase can be induced by temperature, pressure, magnetic field, or doping (4). Normally, the MIT for a band insulator is accompanied by a structural phase transition that changes or breaks the symmetry (5, 6). The simplest example is a one-dimensional chain of atoms, which, as Peierls showed (3), is unstable because of the degeneracy caused by Fermi surface nesting at $2k_F$, where k_F is the Fermi wavevector. The lattice

reconstructs itself, doubling the periodicity and lowering the electronic energy by creating a gap at the Fermi energy (E_F).

In contrast, an inherent Mott transition should be purely electronic in origin and not assisted by a structural transition (1, 2, 5). In practice, almost all of the highly correlated materials with a large enough ratio of U/W to be Mott insulators exhibit close coupling between charge, spin, and lattice, so that the Mott transition is nearly always accompanied by a structure transition. This situation complicates the understanding of the basic mechanism of a Mott MIT as a transition driven by the electron-electron ($e-e$) correlations. We now show that the surface layer of a Mott insulator can display a MIT independent of a structural transition.

The layered ruthenate $\text{Ca}_{2-x}\text{Sr}_x\text{RuO}_4$ shows a rich array of ground states that are associated with the intricate couplings between lattice, electron, and spin degrees of freedom (7–9). Ca^{2+} replacement of Sr^{2+} gradually enhances the rotational and tilt distortion of the RuO_6 octahedra, starting with a tetragonal $I4/mmm$ structure for Sr_2RuO_4 , leading to an $I4_1/acd$ structure for $\text{Ca}_{1.5}\text{Sr}_{0.5}\text{RuO}_4$, and ending with an orthorhombic $S-Pbca$ structure for Ca_2RuO_4 (9). These structural changes lead to an evolution of the ground state, from an unconventional superconducting state in Sr_2RuO_4 (10) to a quantum critical point at $x = x_c \sim 0.5$ (where c is critical) and to an antiferromagnetic Mott insulating phase when $x < 0.2$ (7, 8).

The layered structure of this material, which plays a key role in the anisotropic transport and magnetic properties (7, 8), also makes the crystal

¹Department of Physics and Astronomy, University of Tennessee, Knoxville, TN 37996, USA. ²Department of Physics, Florida International University, Miami, FL 33199, USA. ³Materials Science and Technology Division, Oak Ridge National Laboratory, Oak Ridge, TN 37831, USA. ⁴National Laboratory for Condensed Matter Physics, Institute of Physics, Chinese Academy of Sciences, Beijing 100080, China.

amenable to creating a surface by cleaving and offers a controlled way to investigate the manifestation of broken symmetry on a Mott MIT (11). Bulk studies have demonstrated that the Mott transition in the low Sr-doping regime is intimately related to a structural transition (9). When the system changes from a metallic to a Mott insulating phase on cooling, a concomitant structural transition to a more distorted orthorhombic phase is observed in the bulk. In sharp contrast, we demonstrate here that the Mott transition on a freshly cleaved surface of $\text{Ca}_{1.9}\text{Sr}_{0.1}\text{RuO}_4$ occurs without an accompanying lattice distortion. Our observations and theoretical calculations show that the broken symmetry at the surface creates a structure that allows for an inherent, purely electronic Mott transition. Figure 1 shows unambiguous evidence for a shift of the MIT to lower temperature (T) at the surface of a $\text{Ca}_{1.9}\text{Sr}_{0.1}\text{RuO}_4$ single crystal. The bulk MIT occurs at $T_c = 154$ K (c, critical), as shown by the abrupt change of the bulk electrical resistivity, whereas the surface transition occurs at $T_{c,s} = 130$ K (s, surface), as indicated by the opening of the energy gap measured by scanning tunneling spectroscopy (STS).

To investigate the surface Mott transition as well as the evolution of surface electronic properties and associated lattice dynamics, we have performed both STS and high-resolution electron energy loss spectroscopy (HREELS) measurements versus temperature on the surface of $\text{Ca}_{1.9}\text{Sr}_{0.1}\text{RuO}_4$ (12). Both STS and HREELS are surface-sensitive techniques: STS probes the integrated density of electronic states near E_F , and the spectra from HREELS provide the surface dielectric response through quasi-particle excitations, including phonons and low-energy electron excitations. The low-energy quasi-particle excitations near E_F , referred to as the Drude weight in energy loss spectra, provide a signature of metallicity. The information obtained from HREELS at the surface is similar to that from optical conductivity spectroscopy for the bulk.

The measured T dependence of STS and HREELS spectra shows that both the STS and HREELS spectra display no sign of an energy gap at room temperature (Fig. 2). The HREELS spectra exhibit a sizable Drude weight apparent on the right shoulder of the elastic scattering peak, indicating the metallic character of the surface. The Drude weight decreases gradually with decreasing sample temperature as the elastic peak in the HREELS spectra becomes more and more symmetric. Correspondingly, the density of states near E_F also decreases with decreasing temperature as shown in the tunneling conductance (the derivative of the tunneling current dI/dV) close to zero bias. The energy loss peak at $\hbar\omega_s \sim 81$ meV is an optical phonon associated with the apical oxygen vibration at the surface (13) (\hbar , Planck's constant; ω_s , surface phonon frequency). The corresponding bulk mode is the RuO_6 -stretching A_{1g} mode (Fig. 2B, inset) that appears at a lower energy [$\hbar\omega_b \sim 72$ meV (ω_b , bulk phonon frequency)]

for Ca_2RuO_4 (14). This surface phonon peak gradually decreases its intensity while remaining at a constant energy of ~ 81 meV with decreasing temperature until around 130 K.

Below 130 K, several abrupt changes occur in these spectroscopic measurements that are indicative of a distinct surface transition. An energy gap up to 0.3 ± 0.1 eV emerges in the STS spectra (Fig. 2A), indicating the establish-

ment of an insulating state at the surface below $T_{c,s} = 130$ K. This value of the energy gap is near that measured from the bulk of Ca_2RuO_4 (14–16). The gap of Ca_2RuO_4 obtained from the optical conductivity measurement (14, 15) varies with temperature, from 0.2 ± 0.05 eV at $T_c \sim 356$ K to 0.6 ± 0.03 eV at 11 K. An analysis of the resistivity versus T gives a gap of ~ 0.39 eV for Ca_2RuO_4 (16). Simultaneously,

Fig. 1. Signatures of the MIT in the bulk ($T_c = 154$ K) and at the [001] surface ($T_{c,s} = 130$ K) of a $\text{Ca}_{1.9}\text{Sr}_{0.1}\text{RuO}_4$ single crystal. The T dependence of the bulk resistivity (orange circles and trace) was measured using a physical property measurement system, and the surface energy gap (blue triangles and trace) was measured using a scanning tunneling spectroscopy on cooling. The inset at upper right is a ball model of the unit cell of $\text{Ca}_{1.9}\text{Sr}_{0.1}\text{RuO}_4$. The surface was created by cleavage between two SrO layers without breaking RuO_6 octahedra from the same crystal used for the bulk resistivity measurement.

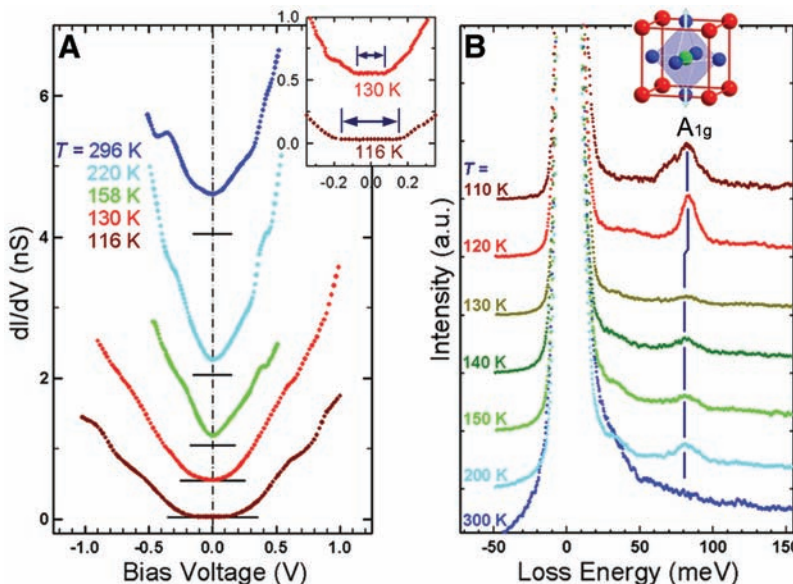
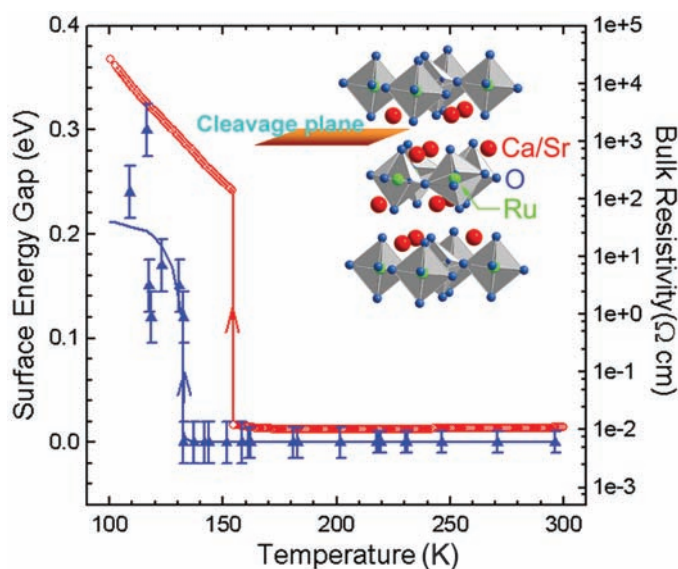


Fig. 2. (A) T dependence of scanning tunneling dI/dV spectra measured at the surface of $\text{Ca}_{1.9}\text{Sr}_{0.1}\text{RuO}_4$ (averaged over an area of $60 \text{ nm} \times 60 \text{ nm}$ by a grid spectroscopic mode with 20×20 sampling pixels, sample bias $V = 1.18$ V, and feedback current $I = 0.76$ nA). The spectra are also shifted for clarity, with the zero value of dI/dV marked by solid lines. The inset is the enlargement of the spectra near E_F showing the opening energy gap (indicated by arrows) when the surface becomes insulating below 130 K. (B) T dependence of normalized HREELS spectra measured at the surface of $\text{Ca}_{1.9}\text{Sr}_{0.1}\text{RuO}_4$ taken with electron scattering at the specular direction. The incident electron beam energy used was 20 eV. The spectra for $T < 300$ K have been incrementally shifted for clarity. The marked peaks are the loss feature due to the optical phonon excitations associated with the RuO_6 stretching mode (see the schematic ball model). a.u., arbitrary units.

the stretching phonon peak shows a shift to higher energy and a sudden increase in intensity in the HREELS spectra (Fig. 2B). In addition, the linewidth of the phonon abruptly changes from ~ 20 meV above 130 K to 7 meV below. This change indicates a coupling between the lattice dynamics and MIT at the surface associated with a change in electron-phonon (e - p) interaction. But, as noted below, the change in the e - p coupling does not drive a structural phase transition at $T_{c,s}$.

To elucidate the correlation of these changes at the surface of $\text{Ca}_{1.9}\text{Sr}_{0.1}\text{RuO}_4$, we have analyzed the STS and HREELS spectra (17) to extract information about the T dependence of the energy gap and the Drude weight, as well as the phonon energy, intensity, and linewidth (Fig. 3) from the data taken on cooling. A sudden drop of the Drude weight and the opening of the energy gap are accompanied by an energy shift, a rapid increase in intensity, and an abrupt linewidth reduction of the surface phonon at the temperature $T_{c,s} = 130$ K, all of which are hallmarks of a surface Mott MIT. The surface MIT temperature ($T_{c,s}$) is more than 20 K lower than T_c (154 K) in the bulk. This finding is counterintuitive, because the conventional picture suggests that e - e correlation effects should be stronger at the surface than in the bulk as a result of the reduced atomic coordination, thus stabilizing the Mott insulating phase and pushing the Mott transition to higher temperatures at the surface as compared to the bulk.

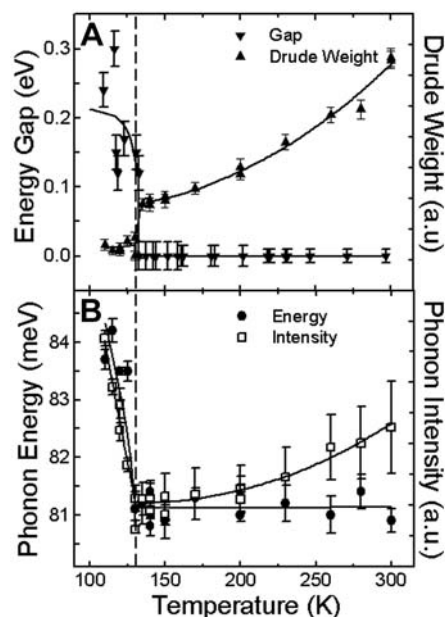


Fig. 3. Sum of the measured results for the surface MIT. **(A)** T dependence of the energy gap determined by the STS spectra and the Drude weight obtained from the HREELS spectra and **(B)** T dependence of the energy and intensity of the optical phonon measured with HREELS at the surface of $\text{Ca}_{1.9}\text{Sr}_{0.1}\text{RuO}_4$. The dashed line marks the surface MIT temperature ($T_{c,s} = 130$ K). The solid lines are guides for the eye.

The bulk first-order Mott MIT in $\text{Ca}_{1.9}\text{Sr}_{0.1}\text{RuO}_4$ is accompanied by an abrupt lattice distortion (9). The bulk structure above and below the bulk MIT, as well as the difference between them, are presented in Table 1. We have determined the surface lattice structure by quantitatively analyzing the low-energy electron diffraction (LEED) I - V (intensity as a function of voltage) spectra (18) at both room temperature (RT) metallic and low-temperature (LT) insulating phases. In order to precisely determine the complex surface structure of this oxide compound, we have used a new self-consistent procedure (19) developed for LEED I - V structural determinations of oxide surfaces. The I - V of 16 nonequivalent beams was measured and compared with calculated intensities for surface model structures. The total I - V energy range (summation of energy ranges for the 16 non-equivalent beams) varied from 3982 to 4469 eV for four sets of data. A good fit with the Pendry reliability factor (20) $R_p = 0.22$ to experimental spectra was achieved, yielding the structure listed in Table 1.

A typical LEED image, which does not change with temperature from 300 to 90 K, is shown in Fig. 4A. The symmetry and the existence of a single glide line in the image pattern indicate a $p(1 \times 1)$ [001] surface of a bulk-terminated orthorhombic structure. This orthorhombic structure (with $Pbca$ space group symmetry) is characterized by a static tilt and rotational distortions of RuO_6 octahedra from the simple cubic perovskite phase. However, the analysis of the LEED I - V data shows that surface structure remains static across both the bulk and surface MIT (Table 1) except for a very gradual thermal relaxation. The comparison of the 90 and 300 K structures reveals no measurable difference (within the error bars). The error bars associated with a change in structure can be reduced by comparing the experimental data below and above the transition. R_p for such a comparison is ~ 0.1 , which allows us to conclude that both the octahedral tilt and the surface buckling remain unchanged within the

error bars ($0 \pm 0.4^\circ$ for tilt and $0 \pm 0.02 \text{ \AA}$ for surface buckling).

Structural distortion is important to create and stabilize a Mott insulating state in the bulk of $\text{Ca}_{2-x}\text{Sr}_x\text{RuO}_4$ (7–9). While keeping the same symmetry, the bulk crystal undergoes a distinct structural transition at T_c that is intimately linked to the MIT (9). This spontaneous structural transition (Table 1) is characterized by a substantial increase in the RuO_6 tilt angle ($\sim 5^\circ$), accompanied by a reduction in the Ru-apical oxygen ion O(2) distances ($\sim 0.05 \text{ \AA}$) and by a considerable increase of the in-plane Ru-O(1) bond lengths ($\sim 0.04 \text{ \AA}$). Similar structural distortions were not observed on the surface; therefore, we were observing a MIT that was solely driven by e - e interactions. All of our structural and spectroscopic data indicate that the surface MIT is of the same nature as the bulk; that is, a Mott MIT. Thus, despite its lower transition temperature (20 K lower), the inherent Mott insulating phase at the surface may be more stable than the inherent Mott insulating phase in bulk, if the bulk structural distortion can be eliminated.

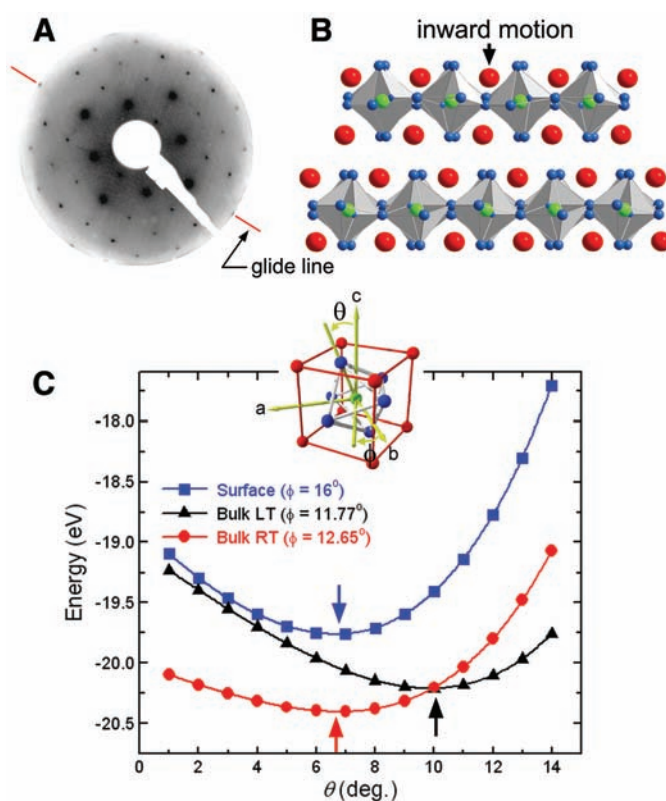
Although in the metallic phase the surface has a slightly larger RuO_6 rotation and tilt than the metallic bulk at room temperature, the observed tilts on the surface never reach the values observed in the bulk insulating phase. As shown schematically in Fig. 4B, the largest surface relaxation is the inward motion of the top Ca/Sr ions (which remains the same at both high and low temperature). This results in a static buckling in the surface Ca/Sr-O(2) layer of 0.23 \AA . The explanation for this compression of the surface layer is straightforward and quite general. When the oxygen above the top Ca/Sr is removed, so is the attractive ionic force that allows the Sr to be pulled inward by the attractive forces from the oxygen below. This type of relaxation has been documented for surfaces of perovskites such as SrTiO_3 (21), BaTiO_3 , and PbTiO_3 (22). This buckling of the surface Ca/Sr-O layer impedes the structural transition that occurs in the bulk at T_c .

Table 1. Comparison between the bulk and [001] surface lattice distortion of $\text{Ca}_{1.9}\text{Sr}_{0.1}\text{RuO}_4$ in orthorhombic structure, mainly the rotational angle (ϕ), tilt angle (θ), and changes of volume of the octahedra. Errors are given in parentheses, with the error bars for the surface measurements determined using R_p (20). The $\Delta_b(\text{LT-RT})$ and $\Delta_s(\text{LT-RT})$ columns are the comparisons of the experimental data between the LT insulating and RT (300 K) metallic phase of the bulk and surface, respectively. Δ_z is the difference in the vertical position between Ca/Sr and the O(2) ions in the surface Ca/Sr-O(2) plane.

	Bulk (9)			Surface	
	T (K)	300	10	$\Delta_b(\text{LT-RT})$	$\Delta_s(\text{LT-RT})$
Ca/Sr-O(2) Δ_z (\AA)		0.159(0.002)	0.179(0.002)	-0.020(0.003)	0.23(0.03)
θ : O(1) (degrees)		6.5(0.1)	11.16(0.05)	4.64(0.05)	9.0(0.7)
θ : O(2) (degrees)		5.2(0.1)	9.40(0.07)	4.1(0.7)	6.8(0.5)
Ru-O(1) (\AA)		1.939(0.002)	1.987(0.002)	-0.048(0.002)	1.97(0.02)
Ru-O(2) (\AA)		1.948(0.002)	1.988(0.002)	-0.040(0.002)	1.98(0.02)
ϕ (degrees)		2.040(0.001)	1.991(0.001)	0.049(0.001)	2.05(0.01)
Volume RuO_6 (\AA^3)		12.65(0.06)	11.77(0.05)	-0.88(0.08)	16(2)
		10.27	10.48	0.21	0(3)
				10.64	-0.02

The above scenario is confirmed by our first-principles calculations using a plane-wave pseudopotential method and local density approximation [see (23, 24) for technique details]. We calculate the total energy as a function of structural distortions, namely RuO_6 rotation and tilting, while fixing the lattice parameters to the experimental ones (neutron diffraction data for the bulk (9) and the LEED results for the surface shown in Table 1). With the bulk structural parameters, our theoretical calculations reproduce the two stable bulk lattice structures (Fig. 4C); one with a tilt angle of $\sim 6.5^\circ$ for the metallic phase and the other with a tilt angle of $\sim 10^\circ$ for the insulating phase. To simulate the situation of the surface, we include the enhanced buckling of the Ca/Sr-O plane in a bulk calculation. As shown in Fig. 4C, this enhanced buckling pins the tilt angle at $\sim 7^\circ$, making the increased tilt energetically unfavorable and inhibiting the structural transition. The calculated tilt angle ($\sim 7^\circ$) is in excellent agreement with LEED $I-V$ -determined results, even though this is not a surface calculation. Although our calculations do not directly account for the broken symmetry of the surface, the search for total energy minima using a bulk calculation including the observed surface structural distortions reveals the influence of the surface enhanced buckling on the ground state structure.

Fig. 4. (A) A typical LEED image at the cleaved surfaces of $\text{Ca}_{1.9}\text{Sr}_{0.1}\text{RuO}_4$ at RT, taken with an electron beam energy of 170 eV. The tilt distortion of RuO_6 octahedra is evident by the existence of only one glide line (on which fraction spots are extinct) instead of two perpendicular glide lines due to the broken symmetry. (B) A ball-model side view of the determined structure from the surface (top layer) to the bulk (bottom layer) of $\text{Ca}_{1.9}\text{Sr}_{0.1}\text{RuO}_4$. The distinct inward motion of Ca/Sr ions at the surface is indicated by the arrow. (C) The calculated total energy versus RuO_6 tilt angle (θ) for three different lattice structures: the bulk RT structure (red symbols), the bulk LT structure (black symbols), and the surface structure (blue symbols). For each case, the calculations were nonmagnetic and were done starting with a bulk structure with the experimentally determined lattice parameters and the rotational angles (ϕ). The inset at top schematically defines the rotation and tilt distortion of RuO_6 octahedron. The arrows indicate the calculated tilt angles (θ) with the minimum energies corresponding to the three structures.



With no structural transition involved in the surface Mott MIT, we can ask what drives the observed inherent Mott MIT at the surface of $\text{Ca}_{1.9}\text{Sr}_{0.1}\text{RuO}_4$. In $\text{Ca}_{2-x}\text{Sr}_x\text{RuO}_4$, three t_{2g} orbitals ($4d_{xy}$, $4d_{yz}$, and $4d_{zx}$) contribute to the electronic states near E_F . In the bulk crystal, both tilt and flattening of the RuO_6 octahedra favor an antiferromagnetic ground state, whereas both tilt and rotational distortion stabilize the insulating phase by narrowing the t_{2g} bandwidth (23, 24). Although never reaching the bulk insulating phase values ($\sim 10^\circ$ on average), the surface tilt angle ($\sim 8^\circ$ on average) is slightly greater than the bulk metallic phase values ($\sim 6^\circ$ on average). In addition, the surface RuO_6 rotational distortion is greater than that in the bulk. All of these factors, plus the reduced coordination at the surface (25–27), which presumably enhances surface correlations, point in the direction of increasing the ratio of correlation to bandwidth (U/W). It is this enhanced ratio that is strong enough to drive the surface Mott MIT without the necessity of a structural transition.

A recent finite-temperature (250 K) multi-band dynamical mean field theory calculation for the Mott MIT in $\text{Ca}_{2-x}\text{Sr}_x\text{RuO}_4$ (28) presents a model that lets us test these assertions. The occupancy of the in-plane d_{xy} band (n_{xy}) is critical for creating the Mott insulating state. We have used density functional theory (DFT) to

calculate n_{xy} for the three relevant structures: (i) the RT bulk (RTB) metallic phase, (ii) the LT bulk (LTB) insulating phase, and (iii) the surface (s), with $n_{xy}(s)$ calculated for a bulk with this structure. The DFT calculation yields $n_{xy}(\text{RTB}) = 0.71$, $n_{xy}(\text{LTB}) = 0.75$, and $n_{xy}(s) = 0.73$. The n_{xy} value for the pure Sr compound is 0.64. This calculation clearly shows the tendency, without any correlation of the three different structures, toward Mott insulator formation. The surface is more susceptible to an inherent Mott MIT than the room-temperature bulk.

The identification of the appropriate microscopic order parameter for a finite temperature MIT has and continues to be actively discussed (29–31). The order parameter associated with an inherent Mott MIT is masked by complications arising from coupled transitions (31). Figure 3 shows that, for the surface inherent Mott MIT, there are several experimental observables that can be configured as order parameters. The normalized gap seen with STS is an appropriate order parameter, as is the gap seen in optical conductivity measurements (29, 30). The Drude weight can be configured to be another order parameter and, because of the strong e - p interaction, the energy and intensity of the optical phonon offer two other physical observables that can be defined appropriately to serve as order parameters. The data in Fig. 3 show how these observables all give the same $T_{c,s}$. Comparison to the first-order structural transition that occurs in the bulk at the MIT temperature indicates that the surface transition may be more gradual. Whether the surface Mott MIT is a second-order phase transition awaits a much more detailed investigation. What is required is a detailed study of the thermal hysteresis of the STS energy gap. However, the bulk first-order character of the Ca-rich single crystals in the $\text{Ca}_{2-x}\text{Sr}_x\text{RuO}_4$ family complicates these measurements. Further experiments are also needed to elucidate the nature of the surface transition. A decisive experiment would be an angle-resolved photoemission study of the evolution of the coherent quasi-particle band as T approaches $T_{c,s}$, especially for $T < T_c$.

References and Notes

- N. F. Mott, *Proc. Phys. Soc. London Sect. A* **62**, 416 (1949).
- N. F. Mott, *Metal Insulator Transitions* (Taylor & Francis, London, 1974).
- R. Peierls, *Quantum Theory of Solids* (Clarendon Press, Oxford, UK, 1955).
- M. Imada et al., *Rev. Mod. Phys.* **70**, 1039 (1998).
- D. Feng, G. Jin, *Introduction to Condensed Matter Physics* (World Scientific Publishing, Singapore, 2005).
- P. W. Anderson, *Basic Notions of Condensed Matter Physics* (Benjamin, Menlo Park, CA, 1984).
- S. Nakatsuji, Y. Maeno, *Phys. Rev. Lett.* **84**, 2666 (2000).
- S. Nakatsuji et al., *Phys. Rev. Lett.* **90**, 137202 (2003).
- O. Friedt et al., *Phys. Rev. B* **63**, 174432 (2001).
- Y. Maeno et al., *Nature* **372**, 532 (1994).
- E. W. Plummer et al., *Surf. Sci.* **500**, 1 (2002).
- High-quality $\text{Ca}_{1.9}\text{Sr}_{0.1}\text{RuO}_4$ single crystals for this study were grown with the use of an optical floating zone furnace, and their bulk properties were in good agreement with reported values (7, 8). The bulk resistivity

was measured with a physical property measurement system. The electrical resistivity shows the MIT at $T_c = 154$ K on cooling (Fig. 1) and exhibits large thermal hysteresis behavior indicating a first-order character of the MIT. $\text{Ca}_{1.9}\text{Sr}_{0.1}\text{RuO}_4$ crystals for scanning tunneling microscopy (STM), LEED, and HREELS measurements were mounted on the sample plates with conducting silver epoxy, and a small metal post was glued on top. The crystal was cleaved by knocking off the post in ultrahigh vacuum with a base pressure of 1.0×10^{-10} torr, producing a flat shiny [001] surface that yielded a sharp LEED pattern. The STM images of the freshly cleaved surfaces show large micrometer-sized terraces. Both the LEED pattern and atomically resolved STM images indicate that the surface has a well-ordered lattice structure. All surface steps are integral multiples of ~ 6.4 Å, which is the spacing between two nearest-neighbor RuO_6 octahedron layers (Fig. 1). LEED I - V analysis shows that the surface is composed of Ca/Sr-O terminations.

13. Ismail *et al.*, *Phys. Rev. B* **67**, 035407 (2003).
14. J. H. Jung *et al.*, *Phys. Rev. Lett.* **91**, 056403 (2003).
15. A. V. Puchkov *et al.*, *Phys. Rev. Lett.* **81**, 2747 (1998).

16. S. Nakatsuji *et al.*, *Phys. Rev. Lett.* **93**, 146401 (2003).
17. Detailed spectral data analysis methods were as follows: The Drude weight is the integrated intensity obtained from the difference between the left and right sides of the quasi-elastic peak through a Lorentzian function. The phonon energy, intensity, and linewidth were obtained by fitting the phonon spectra with a Lorentzian function and were deconvoluted from the Drude tail and instrumentation-resolution function. More details of the surface phonons can be found in (32).
18. M. A. Van Hove *et al.*, *Low-Energy Electron Diffraction Experiment, Theory and Surface Structure Determination* (Springer-Verlag, Berlin, 1986).
19. V. B. Nascimento *et al.*, *Phys. Rev. B* **75**, 035408 (2007).
20. J. B. Pendry, *J. Phys. C* **13**, 937 (1980).
21. E. Heifets *et al.*, *Phys. Rev. B* **64**, 235417 (2001).
22. S. Piskunov *et al.*, *Surf. Sci.* **575**, 75 (2005).
23. Z. Fang, K. Terakura, *Phys. Rev. B* **64**, 020509 (2001).
24. Z. Fang, N. Nagaosa, K. Terakura, *Phys. Rev. B* **69**, 045116 (2004).
25. M. Pattoff, W. Nolting, *Phys. Rev. B* **59**, 2549 (1999).
26. M. Pattoff, *Adv. Solid State Phys.* **42**, 121 (2002).
27. A. Liebsch, *Phys. Rev. Lett.* **90**, 096401 (2003).

28. A. Liebsch, H. Ishida, *Phys. Rev. Lett.* **98**, 216403 (2007).
29. G. Kotliar *et al.*, *Phys. Rev. Lett.* **84**, 5180 (2000).
30. G. Kotliar, D. Vollhardt, *Phys. Today* **57**, 53 (2004).
31. S. Onoda, arXiv: cond-mat/0408297.
32. R. Moore *et al.*, *Phys. Stat. Sol. (b)* **241**, 2363 (2004).
33. Supported by the U.S. Department of Energy (DOE), Division of Materials Science and Engineering, through Oak Ridge National Laboratory. R.G.M. acknowledges support from NSF and DOE (grants NSF-DMR-0451163 and DMS&E). J.Z. thanks NSF for support under contract DMR-0346826. G.T.W. and Z.F. acknowledge support from NSF and the National Basic Research (973) Program of China. We thank A. Liebsch for many informative discussions.

Supporting Online Material

www.sciencemag.org/cgi/content/full/318/5850/615/DC1
Materials and Methods
Figs. S1 to S4
References

18 May 2007; accepted 19 September 2007
10.1126/science.1145374

A Synthetic Lectin Analog for Biomimetic Disaccharide Recognition

Yann Ferrand, Matthew P. Crump, Anthony P. Davis*

Carbohydrate recognition is biologically important but intrinsically challenging, for both nature and host-guest chemists. Saccharides are complex, subtly variable, and camouflaged by hydroxyl groups that hinder discrimination between substrate and water. We have developed a rational strategy for the biomimetic recognition of carbohydrates with all-equatorial stereochemistry (β -glucose, analogs, and homologs) and have now applied it to disaccharides such as cellobiose. Our synthetic receptor showed good affinities, not unlike those of some lectins (carbohydrate-binding proteins). Binding was demonstrated by nuclear magnetic resonance, induced circular dichroism, fluorescence spectroscopy, and calorimetry, all methods giving self-consistent results. Selectivity for the target substrates was exceptional; minor changes to disaccharide structure (for instance, cellobiose to lactose) caused almost complete suppression of complex formation.

Carbohydrates are challenging substrates for host-guest chemistry (1–4). They possess extended, complex structures that require large receptor frameworks for full encapsulation. The differences between them are often subtle (e.g., the stereochemistry of a single hydroxyl group), so that meaningful selectivity is hard to achieve. Most particularly they are found in water and, with their arrays of hydroxyl groups, they quite strongly resemble water. The first task of a receptor is to discriminate between solvent and substrate, and in the case of carbohydrates this is clearly nontrivial. There is evidence that even nature finds the problem difficult. Though critical for many biological processes (5–7), protein/carbohydrate binding is remarkably weak (8). For example, lectins, the most common class of natural receptors, quite often show affinities [association constants (K_a)] of less than 10^4 M^{-1} (9). Previous work on synthetic receptors points in the same direction.

Biomimetic (10, 11) carbohydrate receptors have been sought to model natural recognition and also for applications such as glucose sensing. However, whereas good systems are available for organic solvents (1–3, 12–15), there has been very limited success in water (1–4, 16, 17).

We have targeted carbohydrates with all-equatorial arrays of polar substituents, such as β -glucose **1** (Fig. 1). These substrates have axially directed CH groups, forming small apolar patches at top and bottom. Accordingly, our hosts incorporate roof and floor motifs composed of aromatic hydrocarbons, capable of hydrophobic attraction reinforced by CH– π interactions. These aromatic regions are supported by pillars containing polar groups that can hydrogen bond to the substrate –OH groups (Fig. 1). In prototypes of formula **2**, the roof and floor are provided by biphenyl units, and the pillars are isophthalamides. Recently, we prepared a water-soluble (18–20) variant of **2** and tested its ability to bind carbohydrates in aqueous solution (21). The system was successful but not spectacular. Glucose was bound measurably but weakly ($K_a = 9 \text{ M}^{-1}$) and with moderate selectivity (e.g., glucose:galactose = $\sim 5:1$).

Though encouraging, these properties are hardly comparable to those of lectins.

In biology, most carbohydrate recognition involves oligosaccharides, so we were interested to learn if these extended substrates could be addressed by our strategy (22–26). We therefore considered larger versions of our receptor, aimed at all-equatorial disaccharides such as cellobiose **4** (Fig. 1). We now report the design, synthesis, and study of tetracyclic disaccharide receptor **3**. This host achieves a dramatic leap in performance, showing good affinities and outstanding selectivities for its chosen substrate. It comes remarkably close to true biomimicry and provides a realistic synthetic model for protein/carbohydrate recognition.

Receptor **3** is constructed from two building blocks. A *meta*-terphenyl structure provides the roof and floor, defining the length of the cavity, and isophthalamide units serve as pillars. Each pillar includes two amide linkages, with the potential to hydrogen bond to the –OH groups in **4**. The pillars are also furnished with externally directed tricarboxylate units, to promote solubility and resist aggregation in water. An important consideration was the possibility of cavity collapse, allowing the aromatic surfaces to meet. In aqueous solution, such a process should be strongly favored, driven by hydrophobic interactions. To counter this tendency, the design incorporated five of the rigid isophthalamides, spaced fairly evenly around the terphenyl units. Molecular modeling (27, 28) confirmed that collapsed structures were strongly disfavored; all conformations found within 20 kJ mol^{-1} of the baseline possessed substantial cavities.

The receptor was synthesized from benzenoid precursors via Suzuki-Miyaura couplings and macrolactamizations (29). As expected, it dissolved freely in water to give well-resolved ^1H nuclear magnetic resonance (NMR) spectra, implying a monomeric species (fig. S4). Initial complexation studies were performed using ^1H NMR titrations with cellobiose **4** as a substrate.

School of Chemistry, University of Bristol, Cantock's Close, Bristol BS8 1TS, UK.

*To whom correspondence should be addressed. E-mail: anthony.davis@bristol.ac.uk